RESEARCH ARTICLE

A Solution-Processed All-Perovskite Memory with Dual-Band Light Response and Tri-Mode Operation

Xinwei Guan, Tao Wan, Long Hu, Chun-Ho Lin, Jialin Yang, Jing-Kai Huang, Chien-Yu Huang, Shamim Shahrokhi, Adnan Younis, Kavitha Ramadass, Kewei Liu, Ajayan Vinu, Jiabao Yi, Dewei Chu, and Tom Wu*

Integrating multiple semiconductors with distinct physical properties is a practical design strategy for realizing novel optoelectronic devices with unprecedented functionalities. In this work, a photonic resistive switching (RS) memory is demonstrated based on solution-processed bilayers of strontium titanate ($SrTiO_3$ or STO) quantum dots (QDs) and all-inorganic halide perovskite $CsPbBr_3$ (CPB) with an Ag/STO/CPB/Au architecture. Compared with the single-layer STO or CPB RS device, the double-layer device shows considerably improved RS performance with a high switching ratio over 10^5, an endurance of 3000 cycles, and a retention time longer than 2×10^4 s. The formation of heterojunction between STO and CPB significantly enhances the high resistance state, and the separation of the active silver electrode and the CPB layer contributes to the long-term stability. More importantly, the photonic RS device exhibits UV–visible dual-band response due to the photogating effect and the light-induced modification of the heterojunction barrier. Last, tri-mode operation, i.e., photodetector, memory, and photomemory, is demonstrated via tailoring the light and electric stimuli. This bilayer device architecture provides a unique approach toward enhancing the performance of photoresponsive data-storage devices.

1. Introduction

One of the primary pursuits of current memory technology is high-density data storage. In the last few decades, scientists and industry fields have kept trying to decrease the size of the single memory cell and increase the density of states per single cell by leveraging on multistate approaches.[1] However, with the gradual invalidation of Moore's law and the hard limitation of von Neumann bottleneck, downscaling the size of one unit cell is not a sustainable route because of physical limitations (e.g., current leakage) and fabrication difficulties (e.g., lithography). On the other hand, increasing the number of states per cell becomes a more straightforward and feasible approach to increase storage density. In this context, two-terminal photonic memristors, which combine light illumination as another external stimuli parameter with the conventional electric stimuli, can optically control resistive switching (RS) behaviors at specific wavelengths, enabling the functionalities such as multistate data storage, on-chip integration, and low power consumption.[2]

As a potential candidate for memory applications, oxide perovskites and their derivatives have attracted prodigious attention thanks to their excellent stability, optical transparency, high power efficiency, and simple circuit design.[3–5] Among oxide perovskites, strontium titanate ($SrTiO_3$ or STO) is one of the most promising contenders for next-generation electronics thanks to its unique physical properties, including relatively high dielectric constant, superconductivity, excellent stability, and photocatalytic activity.[6–8] Pure STO has an optical bandgap of 3.2 eV, which renders it a suitable material in visible-blind ultraviolet (UV) photodetection,[9–11] but the conventional bulk device made from STO single crystal is not compatible with the modern semiconductor microfabrication technology.[12] In order to tackle this problem, various techniques have been developed for growing STO thin films.[13–15] As a promising strategy, our previous studies on synthesizing solution-processed STO quantum dots (QDs) provide a low-cost and facile approach to fabricating large-area thin film as the switching media in nonvolatile RS memory applications.[16,17] The solution-based method allows the simple modification of STO properties via doping with transition metal ions (e.g., chromium ions), which helps introduce oxygen-vacancy-dominated switching behavior under an external electric field.[17,18] However, it is still challenging to fabricate single-layer high-performance STO

X. Guan, T. Wan, L. Hu, C.-H. Lin, J.-K. Huang, C.-Y. Huang, S. Shahrokhi, A. Younis, D. Chu, T. Wu
School of Materials Science and Engineering
University of New South Wales (UNSW)
Sydney, NSW 2052, Australia
E-mail: tom.wu@unsw.edu.au
X. Guan, K. Ramadass, A. Vinu, J. Yi
Global Innovative Centre for Advanced Nanomaterials
School of Engineering, College of Engineering, Science and Environment
The University of Newcastle
Callaghan, NSW 2308, Australia
J. Yang, K. Liu
State Key Laboratory of Luminescence and Applications (SKLLA)
Changchun Institute of Optics
Fine Mechanics and Physics (CIOMP)
Chinese Academy of Science (CAS)
Changchun City 130033, China

memory even with these breakthroughs. For instance, the high leaking current owing to the mediocre QD film quality could result in a low ON/OFF ratio.[19] Also, a high voltage is frequently required to facilitate the drift of oxygen vacancies, and the oxygen vacancies can quickly move back when removing the applied voltage, leading to poor endurance and retention performances.[17] Therefore, it is urgent to develop other strategies to boost the performance of STO-based electronics.

During the last decade, hybrid lead halide perovskites ($CH_3NH_3PbX_3$, and X: I^-, Br^-, and Cl^-) have become prevalent because of their remarkable physical properties like ambipolar charge transport,[20,21] long diffusion length,[22] and low trapping density.[23] These characteristics make hybrid perovskites suitable for a broad range of devices, such as solar cells,[24–27] photodetectors,[28–32] light-emitting diodes,[33] lasers,[34,35] transistors,[36,37] and memories.[38–40] Compared with hybrid counterparts, all-inorganic halide perovskites ($APbX_3$, A: Cs or Rb) have demonstrated better phase stability[41] and humidity stability.[42] In previous reports, dual-phase Cs-based perovskites also exhibited improved mechanical stability and surface morphology,[43,44] making them ideal materials for wearable optoelectronics with multimode operation.[45–51] Recently, Hu et al. successfully combined wide bandgap ZnO with phosphorene, and their nano-heterojunctions achieved broadband photonic RS from UV to near-infrared (NIR) with controllable shifts of SET voltages.[52] In our previous study, a layer of $CH_3NH_3PbI_3$ with a strong light response was utilized to extend the light absorption edge of tin monoxide (SnO) phototransistor from UV to the visible spectrum, and significant improvements of photoresponse and field-effect mobility were realized thanks to the favorable band alignment of $SnO/CH_3NH_3PbI_3$ and efficient charge transfer at the interface.[53] Consequently, with appropriate band alignment, the improved RS performance and unique photonic behaviors could be expected by combining STO with all-inorganic halide perovskites, which can also be a potential universal strategy to realize novel optoelectronic functionalities with improved performance.

In this work, we first measure the single-layer RS devices using STO QD film and $CsPbBr_3$ (CPB) thin film as the switching media. Owing to the direct contact of CPB and Ag electrode, the CPB device presents poor stability with awful random jumping during the I–V sweeping, while the STO device suffers from a high current level in high-resistance state (HRS), leading to a low ON/OFF ratio in retention and endurance measurements. On the other hand, the double-layer device with Ag/STO/CPB/Au structure shows considerably improved RS performance thanks to STO/CPB heterojunction formation, which significantly decreases the HRS current level. The double-layer device exhibits a switching ratio over 10^5, an endurance of 3000 cycles, and a retention time of more than 2×10^4 s. More importantly, the photonic RS device consistently reveals a distinct UV–visible dual-band response. Its set and reset voltages can also be reliably modified by changing the light intensity and wavelength owing to the photogating effect and the change of the heterojunction barrier under illumination. Our study demonstrates that the STO/CPB-based memory featuring a dual light response endows the device with an extra tuning parameter, and the double-layer configuration may provide a universal route for enhancing the RS performance.

2. Results and Discussion

The STO QDs were prepared by a sol–precipitation process,[54] and thin films were prepared via a spin-coating method with a thickness of around 70 nm, which is transparent in the visible range with the optical transparency over 90% (Figure S1, Supporting Information). **Figure 1**a presents the morphology of STO QDs with a rectangle shape via transmission electron microscopy (TEM). The fringe spacing of the QDs is 0.28 nm, consistent with the lattice spacing of the (110) plane. Figure S2a (Supporting Information) shows that the size distribution of QDs ranges from 8 to 25 nm, with an average diameter of 16.4 nm. Figure S2b (Supporting Information) presents the X-ray diffraction (XRD) pattern of QD film on a glass substrate, and all the main diffraction peaks can be assigned to the cubic STO phase with a space group of $Pm\bar{3}m$ (JCPDS 35–0734).[17] The absorbance spectrum of STO QDs film is shown in Figure S2c (Supporting Information), and the Tauc plot confirms a bandgap of 3.28 eV, which is consistent with previous sol–gel-derived thin films.[55,56] The top-view scanning electron microscopy (SEM) image (Figure S2d, Supporting Information) demonstrates a dense and smooth STO QD surface with good surface coverage.

The excellent quality of STO QD film enables a reliable application as RS memory. Figure 1b shows the schematic diagram of the STO-based RS memory device, and its sandwich-type architecture of Ag/STO/Au has been confirmed by the side-view SEM image (Figure S3, Supporting Information). Figure 1c depicts the typical RS curve under the voltage sweep sequence of 0 V → 1 V → –0.5 V → 0 V applied to the bottom Ag electrode. An electroforming voltage of 0.82 V is required in the initial sweep, and an abrupt current increase from HRS to low-resistance state (LRS) occurs in the forward bias regime (scan steps 1) as the positive voltage reaches around 0.7 V (set process), while a negative voltage around –0.4 V is needed to reset the device to HRS in scan step 3. The relatively small set/reset voltage can be attributed to the large ion flux caused by the large diffusion coefficient of Ag^+ ions, as illustrated previously.[16,57] It should be noted that we set the compliance current of 10^{-4} A on the forward bias region to avoid the breakdown of the device. The excellent overlap between five I–V loops ensures the device's reliability (Figure 1c), in which the fluctuations of the set and reset voltages are as small as 0.08 and 0.14 V, respectively. Compared to previous reported STO-based RS devices, the switching performance demonstrated here has been dramatically enhanced since a more uniform and thinner STO QD film is employed as the switching media.[17,58] However, the single-layer STO device still suffers from a mediocre ON/OFF ratio of around 10^3 at an applied voltage of 0.5 V due to the relatively high current level of 10^{-7} A at HRS. Moreover, data retention characteristics with a reading bias (V_{read}) of 0.1 V can only be maintained with an ON/OFF ratio of slightly larger than 10^2 in a period of 10^3 s (Figure 1d), and the cycling endurance test (Figure 1e) measured at $V_{read} = 0.1$ V was lasted for only 450 cycles with a small ON/OFF ratio of around 10^2.

The mechanism of the Ag/STO/Au RS device should be linked with the formation and annihilation of metallic Ag filaments in the STO layer,[16,57] as demonstrated in Figure S4 (Supporting Information). When a positive voltage is applied to the
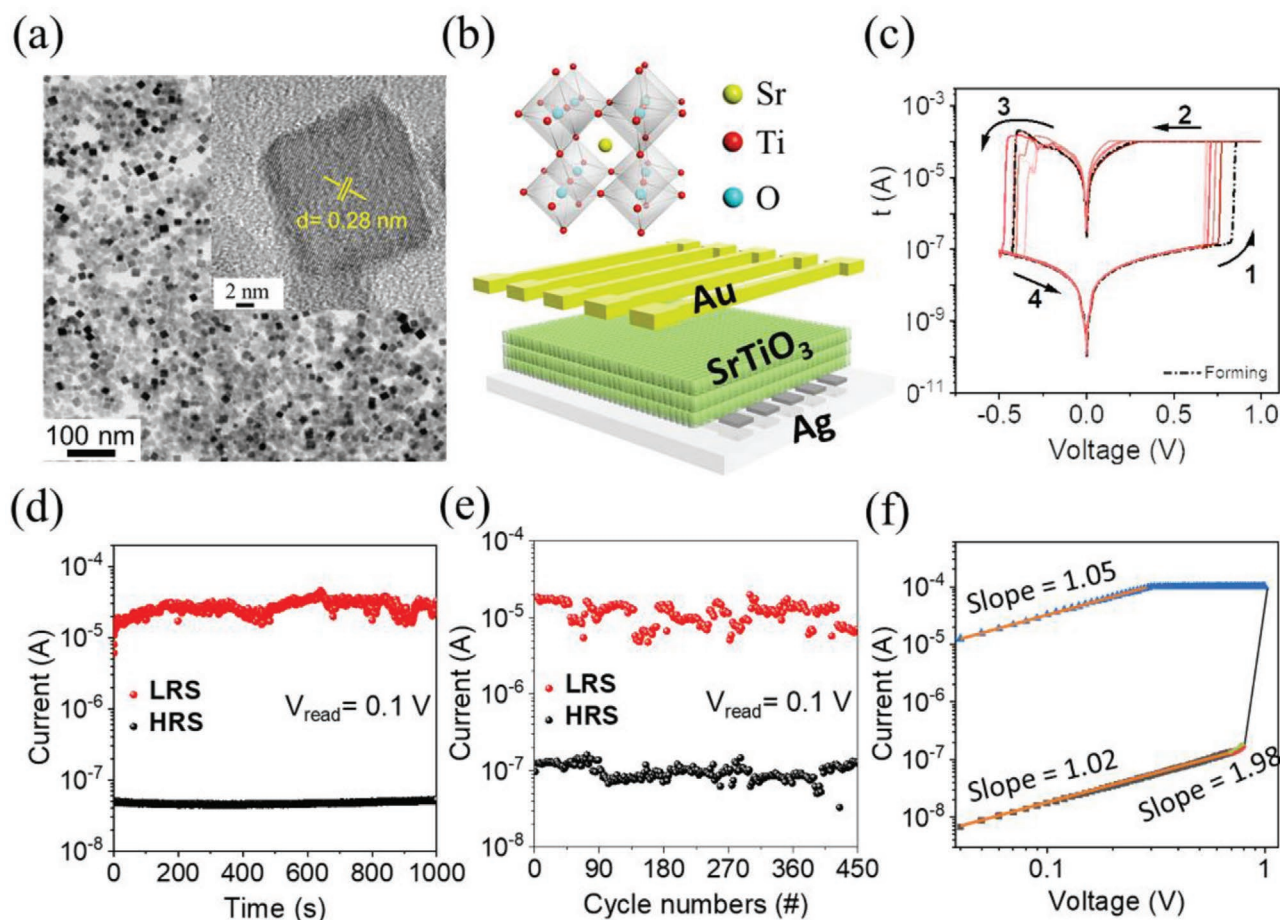
ADVANCED
SCIENCE NEWS
www.advancedsciencenews.com

ADVANCED
FUNCTIONAL
MATERIALS
www.afm-journal.de

Figure 1. a) TEM and high-resolution TEM (HRTEM) images of STO QDs. b) Schematic illustration of the single-layer STO device. c) I–V loops of the Ag/STO/Au device. d) Retention and e) endurance results of the single-layer STO device. f) The replotted I–V curve in the log–log scale in the positive voltage sweeping region.

Ag bottom electrode, Ag atoms tend to be dissolved in the STO QDs' layer as Ag cations, and then subsequently diffused toward the top Au electrode by the electric field and reduced back to Ag atoms. The reduction of Ag cations is promoted with electrons from the Au cathode, so Ag filaments begin to grow near the top electrode and gradually connect two electrodes, leading to the transition from HRS to LRS. Notably, the set voltage (0.7 V) and its corresponding electric field (10 V µm^{-1}) can support the migration of Ag cations.[59] On the contrary, when a negative bias is applied to the Ag electrode, the conducting filaments are abruptly dissolved due to Joule heating, and the device switches back to HRS. To further understand the conduction mechanism, the log–log scale of the I–V curve is replotted in Figure 1f. In the HRS, the fitting result indicates that the charge-transport behavior follows a typical trap-controlled space-charge limited current (SCLC) mechanism, which is consisted of an Ohmic region ($I \propto V$), a Child's region ($I \propto V^2$), and a sudden current increase region.[60] In the low-voltage region from 0 to 0.7 V, the conduction is mainly dominated by thermal-generated carriers trapped in the STO layer. In this region, the trap sites are not fully filled because of the weak electron injection from the Au electrode, leading to the Ohmic conduction. After voltage gradually increases (from 0.7 to 0.8 V), the injected carriers domi-

nate the conduction mechanism, and the trapping/de-trapping of injected carries by the inherent defects in the STO makes the current flow proportional to the square of the bias voltage, labeled by the orange color in Figure 1f. Afterward, the device goes through the sharp current increasing region, and the mechanism should be the conduction through Ag filaments, which are confirmed from the Ohmic conduction in the LRS with a slope of 1.05. We characterized dozens of devices with different electrode areas. As displayed in Figure S5 (Supporting Information), the resistance value of Ag/STO/Au RS memories presents an inverse linear dependence on the electrode area in the HRS. In contrast, the resistance value in the LRS is independent of the cell size, indicating that the RS occurs due to the conducting filaments within the STO QDs layer.[38,57]

The single-layer CPB devices were also fabricated and studied. A 160 nm CPB thin film was sandwiched between the Ag and Au electrodes with Ag/CPB/Au structure (**Figure 2**a; Figure S6, Supporting Information), and the top-view morphology of CPB was studied by SEM (Figure 2b), where no pinhole has been found with the average grain size of around 0.4 µm. XRD measurement (Figure 2c) demonstrates that the CPB film is polycrystalline and single phase with a cubic structure. Figure 2d displays five successive I–V curves of the as-fabricated CPB device under the voltage

**ADVANCED
SCIENCE NEWS**

www.advancedsciencenews.com

**ADVANCED
FUNCTIONAL
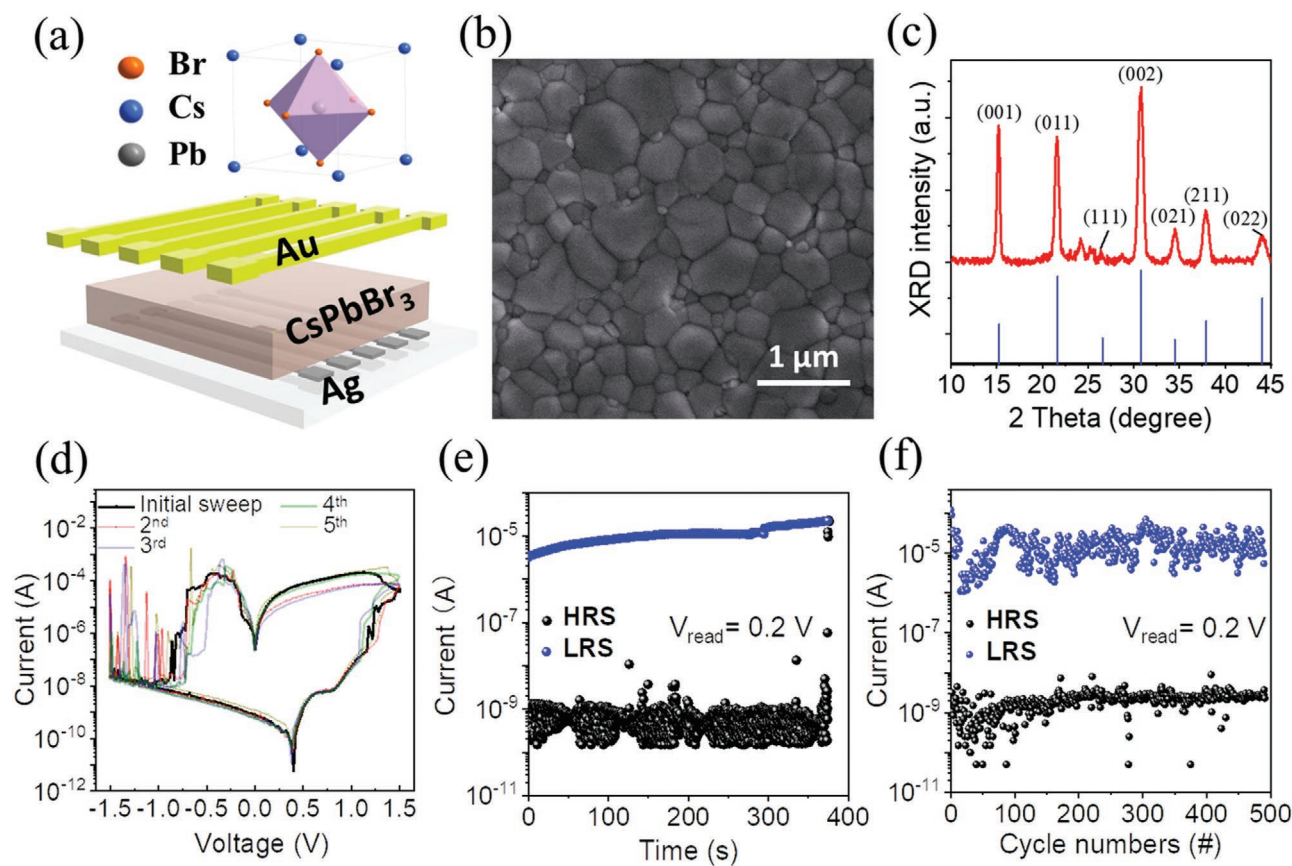MATERIALS**

www.afm-journal.de

Figure 2. a) Schematic diagram of the single-layer CPB device. b) Top-view SEM image and c) XRD pattern of the CPB thin film on the glass substrate. d) I–V loops for five switching cycles of the Ag/CPB/Au device. e) Retention and f) endurance measurements of the single-layer CPB device.

sweep sequence of 0 V → 1.5 V → 0 V → −1.5 V → 0 V. Compared to STO devices, the single-layer CPB device exhibits a better ON/OFF ratio of around 10^4 without the electroforming process.[61,62] The formed Ag filaments and bromide vacancy filaments within the CPB layer could be responsible for the RS behavior.[45,58] However, the device presents extremely unstable electrical behavior, and the resistance states seriously jump up and down at the negative bias region. The retention (Figure 2e) and endurance (Figure 2f) measurements also confirm the unstable nature of the CPB device, where its HRS can only last for 373 s and 491 cycles, respectively.

Previous works have reported severe reactions and damages occurring at the Ag/perovskite interface.[45,59] As an exemplary remedy approach, an extra passivation layer (e.g., polymethyl methacrylate (PMMA)) was inserted between perovskites and Ag electrodes.[63] To solve this problem while gaining additional functionality, we integrated the CPB layer with the STO QDs' layer in an all-perovskite bilayer heterostructure. The benefits are two folds: the STO layer separates the CPB from the Ag electrode, thereby enhancing the device stability; and the light response property is also enriched since the STO and the CPB layers have different optoelectronic characteristics. In our previous work, STO has been proven to be an effective electron-transport material in organolead trihalide perovskite solar cells,[64] which motivated us to integrate oxide perovskite STO with halide perovskite CPB in a photonic RS memory device.

Figure 3a depicts the architecture of the STO/CPB hybrid device, and the side-view SEM image shown in Figure 3b clearly reveals its double-layer heterostructure. The thicknesses of the CPB and STO layers are 160 and 70 nm, respectively. The thin STO layer is critical for a stable device operation since it separates the CPB layer from the Ag electrode and prevents any halide–metal reaction at the interface. Moreover, adding the STO layer enhances the photoresponse in the UV regime, which will be discussed later. Notably, there is a tradeoff regarding the CPB thickness: a thick layer will lead to strong light absorption and photoresponse, but it must be thin enough to prompt filament formation/rupture with a relatively low external bias. Additionally, both layers must reach certain thicknesses with optimized coating conditions in order to minimize the pinhole formation. The top-view morphology of CPB on the STO layer is presented in Figure S6 (Supporting Information), which has no noticeable morphology difference with the film grown on glass substrate but with a slightly smaller grain size of around 0.29 µm. It is worth mentioning that a considerable photoluminescence (PL) quenching (over 85%) was observed in the STO/CPB composite, suggesting an effective carrier transfer between the CPB and STO layers (Figure 3c).[64] We believe that this effect is because STO provides a favorable energy level gradient for the CPB, dramatically enhancing the electron-transfer process (Figure S7, Supporting Information). Under dark, charge transfer at the STO/CPB interface leads
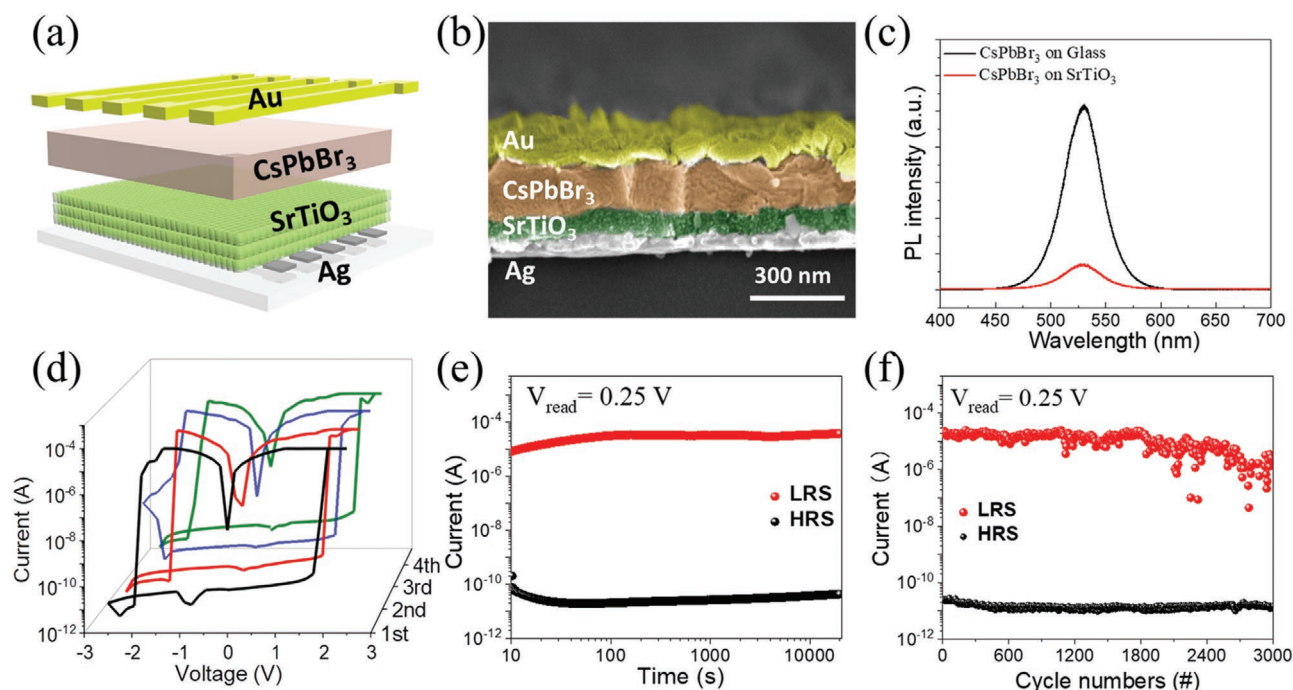
Figure 3. a) Schematic diagram of the two-terminal RS device with the Ag/STO/CPB/Au structure. b) Cross-sectional SEM image of the bilayer STO/CPB device. c) Photoluminescence spectra of CPB on glass and CPB on STO QDs' film. d) Typical I–V curves of the STO/CPB heterojunction. e) Retention and f) endurance characterizations of the double-layer STO/CPB hybrid device.

to the formation of large depletion regions, so these depletion regions along with the Schottky barrier at the Au/CPB and Ag/STO interfaces suppress the dark current in the heterostructure bilayer, resulting in the low current level in HRS. In contrast, under light illumination, large amounts of electron–hole pairs are generated in the CPB layer (and STO layer with high-energy UV illumination). Those electrons are then transferred to the STO QDs' layer, resulting in the reduced heterojunction barriers at the contact interface and high photocurrent, further promoting the filament formation in the double-layered device.

To prove this hypothesis, typical I–V characterizations of the STO/CPB device are measured, as displayed in Figure 3d. Voltage is swept by applying 0 V → 2.5 V → −2.5 V → 0 V with 10^{-4} A compliance current, and a vastly improved and stable ON/OFF ratio of $>10^5$ has been observed. The ON and OFF switching processes occur at a SET voltage of around 1.7 V and reset voltage of around −1.4 V. Interestingly, compared with single-layer devices, HRS current decreases from 10^{-7} (10^{-8}) A for the STO (CPB) device to 10^{-11} A for the double-layer device (Figure 3d). The series circuit of the STO and CPB layers significantly increases the resistance of the device, and their formed heterojunction (Figure S7, Supporting Information) effectively separated the inherit carries in STO QDs' film, thus avoiding high current at HRS before the device converts into LRS and resulting in a much better ON/OFF ratio. In addition, the narrow bandgap of CPB pledges the double-layer device to absorb the light with a wavelength shorter than 531 nm (2.33 eV), which considerably broadens its utilization potential. Moreover, the I–V characterization of the STO/CPB device with inert Au electrodes, in comparison with the case of Ag electrodes, is displayed in Figure S8 (Supporting Information). Instead of the filament-type RS, an interface-type behavior was

observed, demonstrating that the formation and annihilation of Ag filaments dictate the RS behavior of the devices with Ag electrodes.

The double-layer hybrid device with a larger thickness also presents improved retention and endurance performance. The retention characterization of the hybrid device is measured at $V_{read} = 0.25$ V (Figure 3e), where the HRS and LRS can be maintained for 2×10^4 s at an ON/OFF ratio of $>10^5$. Under the same read voltage, endurance is measured up to 3000 cycles with an ON/OFF ratio of 10^5 (Figure 3f). Even though the switching cycles are maintained approximately with 10^{-5} A at LRS and 10^{-11} A at HRS, there is a fluctuation in LRS, possibly owing to the incomplete formation of Ag filaments since the larger thickness of the double-layered device may hinder the formation of metal cation conductive filaments (CFs).[58] Nevertheless, the retention, endurance, and stability performance of the double-layered device significantly outperform the single-layer counterparts. Notably, compared with single-layer STO/CPB devices, the required power for switching the double-layer device increases due to the thicker switching medium (Figure S9, Supporting Information). The performance comparisons between the single-layer and double-layer devices and other typical Cs-based perovskite memories are summarized in **Table 1**, indicating that the performance of the double-layer device is outstanding and promising.

STO has widely been studied as the active material in visible-blind UV photodetectors by reason of its wide optical bandgap of 3.2 eV,[9,12,76] while CPB with the bandgap of 2.3 eV has been utilized in visible-range applications.[45,77] Therefore, it is presumed that RS properties of the double-layer STO/CPB device exhibit the UV–visible dual light response. In this work, we use a 30 nm thick semitransparent Au layer as the top electrode

Table 1. Comparison of the RS performance of single-layer and double-layer inorganic halide perovskite memories.

Device structure	V_{set}/V_{reset} [V]	I_{on}/I_{off}	Endurance [times]	Retention [s]	Mechanism	Year	Ref.
Polyethylene terephthalate (PET)/indium tin oxides (ITO)/$Cs_3Bi_2I_9$/Au	0.3/−0.5	10^3	10^3	10^4	V_I CFs	2017	[65]
Fluorine-doped tin oxide (FTO)/$CsPbBr_3$/ZnO/Ni	□±1	10^5	–	10^4	Interface type	2017	[66]
$Si/SiO_2/Ti/Pt/Cs_3Bi_2I_9$/Au	0.1/−0.27	9.73×10^8	400	10^3	V_I CFs	2018	[67]
ITO/$CsPbCl_3$ QDs:PMMA/Al	−0.3/2.6	2×10^4	100	10^4	Trap-controlled SCLC	2018	[68]
ITO/$CsPbBr_3$ QDs/Au	1.5/WORM	10^4	–	10^3	Trap-filled SCLC	2019	[69]
ITO/$CsBi_3I_{10}$/Al	−1.7/+0.9	10^3	150	10^4	V_I CFs	2019	[70]
$Si/SiO_2/Ti/Pt$/poly(3,4-ethylenedioxythiophene) polystyrene sulfonate (PEDOT:PSS)/Cs_4PbBr_6/Au	0.6/−0.8	100	100	10^4	V_{Br} CFs	2019	[71]
ITO/PEDOT:PSS/Cs_4PbBr_6/Au	0.5 to 2.0/−0.6	60	100	10^4	V_{Br} CFs	2019	[72]
Pt/$CsSnI_3$/PMMA/Ag	0.13/−0.08	7×10^3	600	7×10^3	Ag CFs	2019	[73]
Pt(ITO)/$CsSnI_3$/PMMA/Au	–	10^3	120	10^4 (ITO)	Interface type		
FTO/$Cs_3Bi_2I_9$/Ag(AgO$_x$)	−0.12/1.0	10^3	250	≈10^6	CF ($V^{\cdot}_I$)	2020	[59]
FTO/$CsBi_3I_{10}$/Ag(AgO$_x$)	−0.14/0.55	<10^3	250	≈10^6			
Au/$Cs_3Sb_2Br_9$ (5 μm)/Au	2.1/−4.5	10^6	–	2×10^4	V_{Br} CFs	2020	[74]
Au/$Cs_3Sb_2Br_9$ (10 μm)/Au	±2.6/volatile	10^3	200	–			
ITO/PEDOT:PSS/CuSCN/$CsPbBr_3$/Au	–	2–6	2×10^3	–	Charge trapping/de-trapping	2020	[75]
Ag/$SrTiO_3$/Au	0.7/−0.4	<10^3	450	>10^3	Ag CFs	2021	This work
Ag/$CsPbBr_3$/Au	1.1/−0.6	10^4	491	373	Ag CFs	2021	This work
Ag/$SrTiO_3$/$CsPbBr_3$/Au	1.7/−1.4	10^5	3×10^3	2×10^4	Ag CFs	2021	This work

with average light transmittance values of 14.5% and 25.1% at the wavelengths of 365 and 505 nm, respectively (Figure S10, Supporting Information), and the sheet resistance (R_s) of the 30 nm thick Au film is ≈14 Ω/□, which is consistent with the previous literature.[78] Without light illumination, the device keeps in HRS during the voltage-sweeping process from 0 to 1.7 V (Figure 3d). Nevertheless, its HRS current increases from 10^{-10} to 10^{-9} A under the external light illumination (2 mW cm^{-2}) with a wavelength of 505 nm, and the HRS current can be further boosted to 10^{-8} A under UV light illumination (365 nm) with the same light power intensity, as shown in **Figure 4**a. Since the small external bias cannot move the metallic ions or halide defects, the current increase in HRS under illumination should be attributed to the photoelectric effect, while 505 nm green light can only be absorbed by the CPB layer (Figure S11, Supporting Information). Under green light illumination, the carrier concentration in the perovskite is greatly increased, thus significantly decreasing the resistance of the CPB layer, but the STO layer remained at a high-resistance level, leading to relatively high series resistance. On the other hand, the high-energy UV light with a wavelength of 365 nm can be absorbed by both halide perovskite and oxide perovskite; so, a large number of photogenerated carriers are generated in both layers, resulting in a higher current in HRS.

As shown in Figure 4a, the bilayer RS device remains in HRS under dark when the sweeping voltage is in the range from −1 to 1 V. Remarkably, it abruptly switches into LRS at a voltage bias of around 0.50 V (0.43 V) when the light illumination is applied with a wavelength of 505 nm (365 nm). Besides, we can observe some intermediate resistance states occurring

during the setting process upon light irradiance. To further understand the photonic properties of the hybrid RS device, the 505 and 365 nm light with different power intensities ranging from 0 to 2 mW cm^{-2} are applied. As shown in Figure 4b, during the set process, the voltage required to switch the device steadily decreases from 1.49, 1.34, 1.12 to 0.50 V when the green light (505 nm) illumination intensity is increased from 0 to 2 mW cm^{-2}. UV illumination induces more substantial negative shifts of set voltage than the green light (Figure 4c), from 1.47, 0.94, 0.55 to 0.41 V with the same irradiation intensities. The relationship between the set voltage and light intensity is summarized in Figure 4d, which highlights the decrease of set voltage by increasing illumination intensity. Similarly, after programming the device to LRS, the voltage required to reset the device increases from −0.62 to −1.17 V and from −0.41 to −1.20 V with decreasing light power intensity of green light and UV light, respectively (Figure 4e,f). The relationship between the reset voltage and illumination intensity is concluded as well in Figure 4g.

To fully utilize the photoresponsive functionalities of the double-layer devices, we further conducted endurance measurements by systematically modifying the light wavelengths and intensity of the external illumination. We first adjusted the illumination wavelengths with a fixed light intensity of 2 mW cm^{-2}. The distribution of multilevel HRS upon 60 writing cycles is displayed in Figure 4h, where distinct HRS can be found under dark and with different wavelengths from 620 to 340 nm. However, the current of LRS remains roughly the same since Ag filaments dominate the resistance value when the device is switched on, and the initial states can be fully recovered when
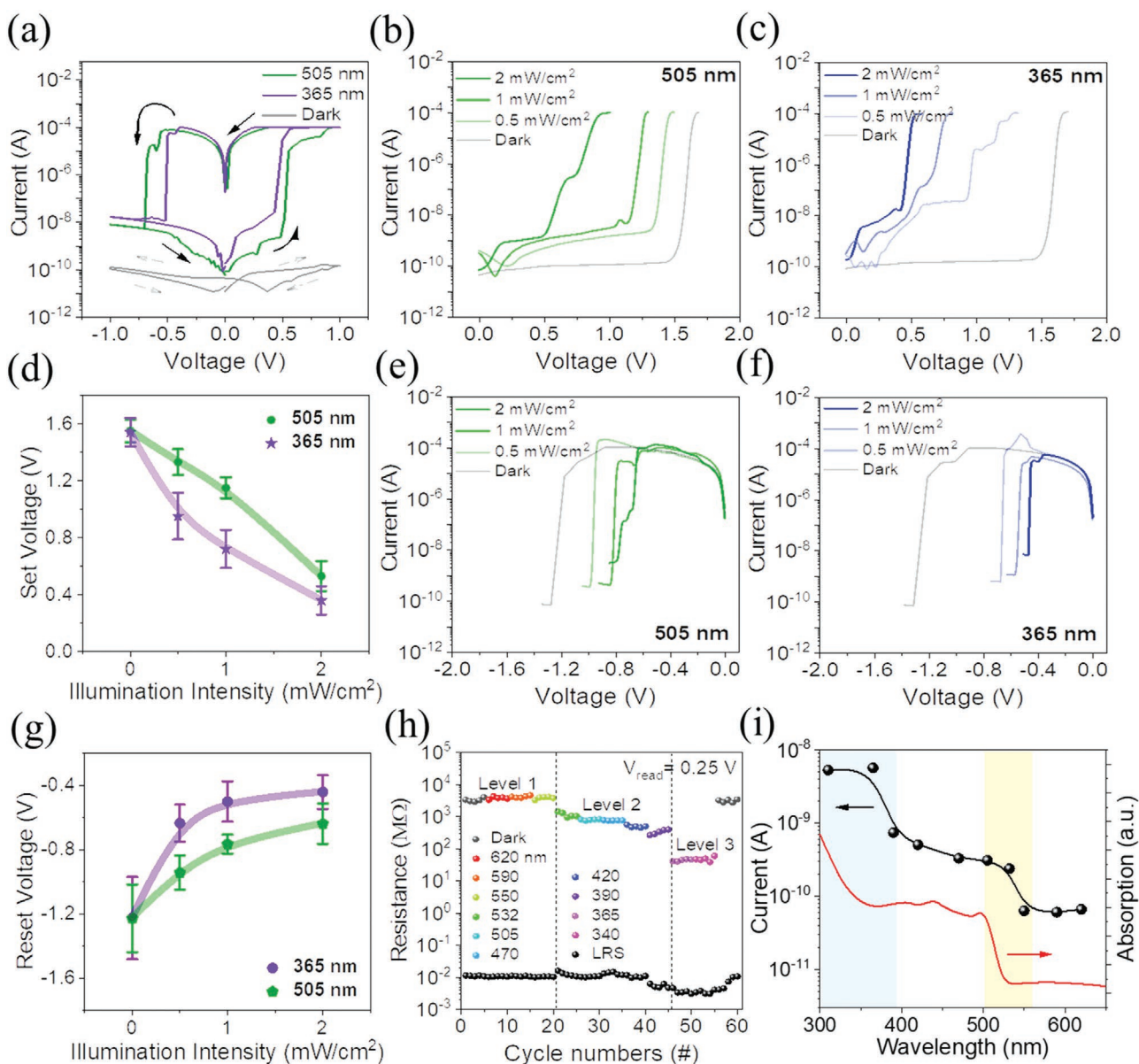
Figure 4. a) Typical *I–V* characteristics of the Ag/STO/CPB/Au device. The light power intensity is 2 mW cm⁻² at 505 and 365 nm. Set processes with different illumination intensities at b) 505 nm and c) 365 nm, respectively. d) Dependence of the SET voltage on illumination intensity. Reset processes with different illumination intensities at e) 505 nm and f) 365 nm, respectively. g) Dependence of the reset voltage on illumination intensity. h) Reversible RS of 60 cycles under dark and with different wavelengths (2 mW cm⁻²) from 340 to 620 nm. i) Corresponding photocurrent of the Ag/STO/CPB/Au device along with its absorption spectra.

the light is turned off. Owing to the optical bandgaps of STO and CPB, light illumination with a wavelength from 550 to 620 nm does not change the device's resistance, while photons from 390 to 532 nm can only be absorbed by the CPB layer. Only high-energy UV light (365 and 340 nm) can be absorbed by both two layers. Therefore, at least three differentiable OFF states can be separated in the double-layer device by controlling illumination wavelength. The corresponding photocurrent and absorption of the STO/CPB device are presented in Figure 4i, which directly illustrates the dual-band property of the double-layer device and agrees well with the wavelength-dependent responsivity measurement given in Figure S12 (Supporting

Information). Next, we demonstrated the distinctly diverse resistance states under different light illumination irradiance, as shown in Figure S13 (Supporting Information). Five unique resistance states can be achieved by tuning UV (365 nm) light intensity from 0 to 2 mW cm⁻² for multilevel data storage.

The above results indicated that light illumination could facilitate the formation and rupture of Ag conductive paths in the CPB/STO device, and high-energy UV light has a more substantial effect than green light. This phenomenon is quite different from previous work based on halide vacancy or interstitial filaments, where a noticeable increase of set voltage and decrease of reset voltage were realized by increasing light

intensity because the iodine-vacancy-based filaments become unsteady under illumination.[79] In our case, the double-layer device can be considered as a special series circuit connection, and the bias applied to it was distributed on the STO and CPB layers according to their resistance ratio. Under dark, the voltage dropped across the CPB layer was high due to its high resistance, and the electric field distributed to the STO layer was not strong enough for Ag dissolution and migration. As a result, a relatively large external electrical bias is required to activate the filament formation process. Under this circumstance, after the Ag dissolution from the electrode, the strong electric field swiftly pushes Ag cations toward the Au electrode, so we observed a quick jump from HRS to LRS without intermediate resistance states in $I–V$ curves (Figure 3d). Under illumination, on the other hand, the set voltage has been considerably decreased, and the Ag filament formation process could be divided into two parts (Figure S14, Supporting Information): the filaments were first formed in the CPB layer, causing a current jump stage in the $I–V$ curve. At this stage, the whole applied voltage dropped across the STO layer only. Then filaments further grew into the STO layer and connected both

electrodes, resulting in LRS of the entire device and causing the intermediate resistance states. Due to the vertical structure of the device, around 70% of the incident photons were blocked and absorbed by the top electrode, so light intensity affected significantly on the above-mentioned process.

Two mechanisms may concurrently contribute to the photoresponse of the double-layer hybrid device. The first one is the photovoltaic effect since the Au/CPB/STO/Ag heterojunction resembles a solar cell device and facilitates the extraction of photocarriers.[45,52] As illustrated in **Figure 5**a, CPB and STO form a type-II band alignment under dark, and the current goes through the heterojunction is small because of the high energy barrier. Ag atoms are slowly dissolved into Ag cations and then reduced back into Ag atoms at the Au electrode under the external bias. Under the green light illumination, the CPB layer absorbs the photons and generates electron–hole pairs (Figure 5b). Some electrons drift to the CPB/Au interface under the influence of the external electric field and get trapped there, providing an additional internal electrical field. This induced photogating effect, in addition to the photovoltaic effect, accelerates the movement of Ag$^+$ toward the cathode,
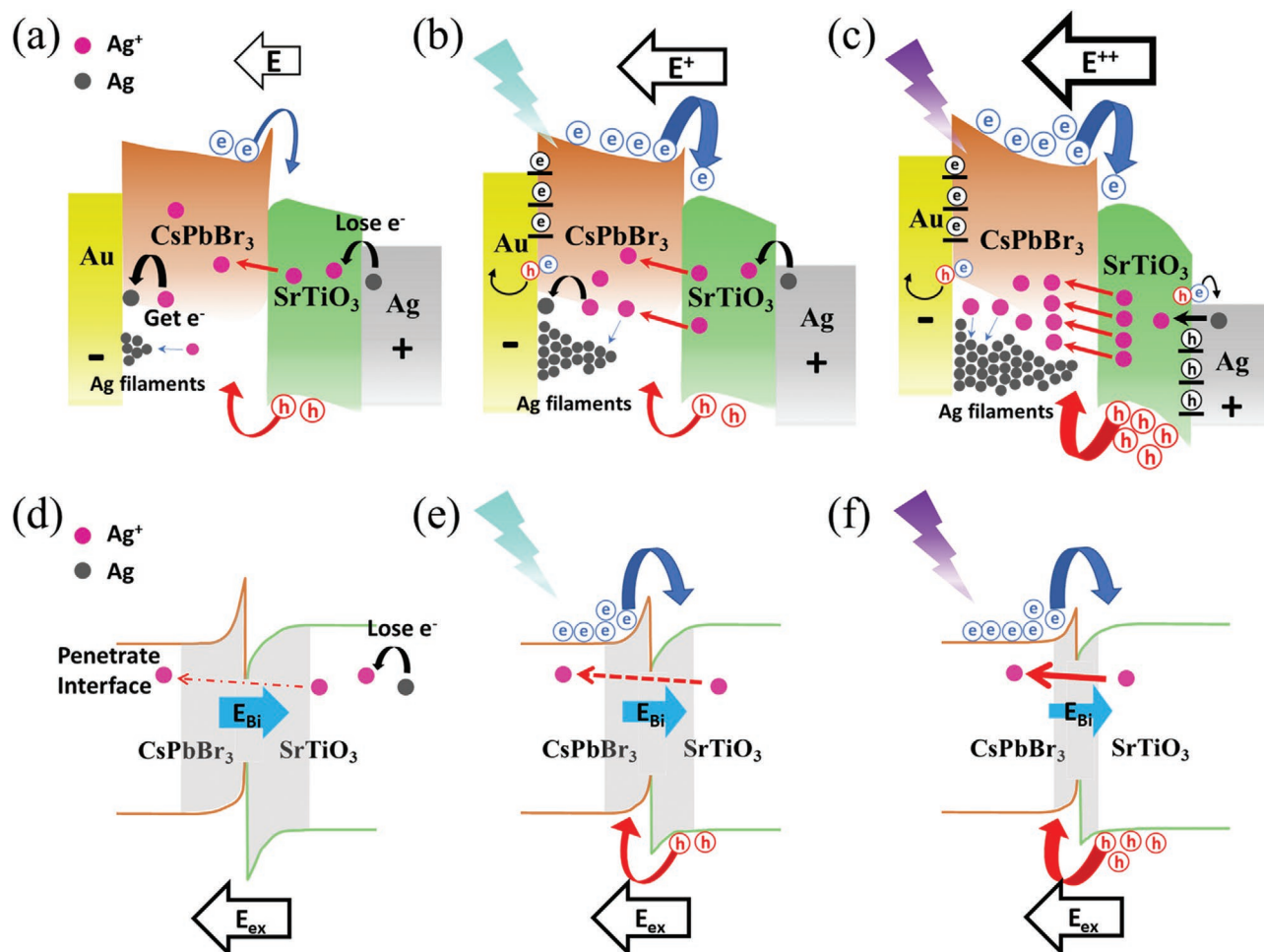

Figure 5. Schematic illustration of the proposed photonic RS mechanism. Energy diagram of the double-layer device during the SET process under a) dark, b) green light (505 nm), and c) UV (365 nm) illumination. The photoexcited carriers can assist the Ag redox reaction and facilitate the filament formation. The thickness of the depletion layer at the CPB/STO heterojunction gradually decreases from d) dark condition to e) under green light illumination, and f) under UV illumination.

ADVANCED
SCIENCE NEWS
www.advancedsciencenews.com

ADVANCED
FUNCTIONAL
MATERIALS
www.afm-journal.de

thus promoting the Ag filament formation. On the other hand, UV photons have higher energy and can be absorbed by both layers, as shown in Figure 5c. Consequently, more photo-generated holes can be arrested at the STO/Ag interface, generating a higher internal electric field. In addition, the change of the STO/CPB heterojunction barrier could also contribute to the photonic behavior of the RS device. The built-in electric field within the depletion region hinders the movement of Ag^+ ions, as illustrated in Figure 5d, but the light illumination can narrow the depletion region and decrease the built-in electric field.[2] Only the CPB layer responds to the green light illumination (Figure 5e), while the UV light generates carries in both layers, further narrowing the depletion region (Figure 5f). In the reset process, the photogenerated holes can promote the dissolution of Ag filaments, decreasing the reset voltage for the filament rupture. UV photons have higher energy than the green ones and generate more photocarries, leading to a smaller reset voltage.

The synergistic combination of halide perovskite and oxide perovskite bilayers warrants the multifunctionalities of the CPB/STO device. Here, we further exploit its functionalities by demonstrating three working modes under different light and electric conditions, i.e., photodetector mode, memory mode, and photomemory mode. First of all, both STO and CPB can behave as light-sensing materials so that the double-layer device can work in the photodetector mode. In our case, we found that reliable responses to light illumination could be achieved for multiple cycles under a limited external bias (e.g., 0.1 V), as depicted by temporal photoresponse measurement in **Figure 6**a. Both layers can absorb the UV light, therefore, generating more carriers and achieving higher photocurrent than green light illumination. The small bias excludes the possibility of ions movement, so no filaments can be accumulated, and the device works in HRS during the whole process. The transient photocurrent characteristic of the CPB/STO device has also been tested with a pulsed laser at 365 nm to investigate the speed performance. As displayed in Figure S15 (Supporting Information), the rise time (from 10% to 90%) and decay time (from 90% to 10%) are 60 ns and 264.5 μs, respectively. The response speed of the CPB/STO device approaches the experimental limitation because the pulse width of the pulsed excitation laser is around 10 ns (10 Hz and 365 nm). The speed measurement was performed under a bias of 0.1 V, and a higher pulse could further increase the response speed, indicating that our device is promising for high-speed optoelectronics.

On the other hand, as shown in Figure 6b, when a strong voltage pulse (e.g., 3 V and 0.5 s) is applied, an abrupt current increase from 10^{-10} A (HRS) to 10^{-4} A (LRS) is observed.
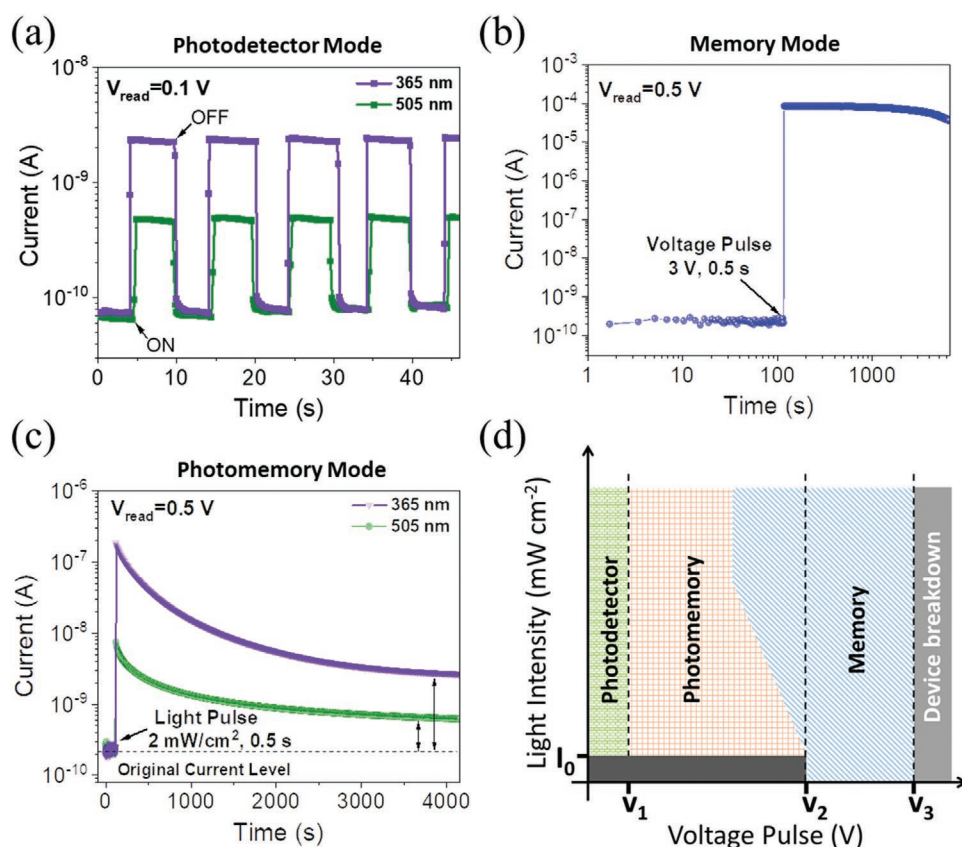

Figure 6. Tri-mode operation of the bilayer CPB/STO device. a) Time-dependent photocurrent response of the double-layer device under a small bias ($V_{read} = 0.1$ V) and chopped light irradiation (intensity: 2 mW cm^{-2}), which represents the photodetector mode. b) Retention ($V_{read} = 0.5$ V) of the current in the memory mode after a voltage pulse stimulation ($V_{pulse} = 3$ V, 0.5 s). c) Retention ($V_{read} = 0.5$ V) after a light pulse stimulation (2 mW cm^{-2}, 1 s) with two different wavelengths, illustrating the photomemory mode. d) Summary of the working modes, i.e., photodetector, memory, and photomemory, as well as their operating conditions.

ADVANCED
SCIENCE NEWS
www.advancedsciencenews.com

ADVANCED
FUNCTIONAL
MATERIALS
www.afm-journal.de

Clearly, the device works in the memory mode since the bias is higher than the setting voltage (≈1.7 V, as shown in Figure 3d). The LRS is stable and can be sustained for more than 1000 s. In this operation mode, the large external bias can easily lead to the movement of Ag ions and result in filament formation regardless of light irradiation.

Intriguingly, with appropriate electric bias (e.g., 0.5 V), the double-layer device is able to work in the photomemory mode (Figure 6c). The external light pulse quickly pumps up the current level from 10^{-10} to 10^{-7} (10^{-8}) A with UV (green light) illumination. Thereafter, the current gradually decreases and then stabilizes, while the final stabilized current is more than ten times higher than the original current level (three times for green light). This programming current can be retained for more than 4000 s. Under this circumstance, the electric bias alone could not cause ion movement, but the light pulse decreases this threshold and activates the process, as aforementioned. The slow relaxation process should be related to the gradual ions' back diffusion after removing the light pulse, but filaments could be partially retained and contribute to the long-term final current level thanks to the nonvolatile properties (Figure S14, Supporting Information). Due to the mechanisms introduced in Figure 5, UV light can cause more robust filaments than green light, resulting in a higher stabilized current level in the end. Notably, a negative voltage pulse can quickly reset the device to its original state (Figure S16, Supporting Information).

Figure 6d summarizes three working modes, i.e., photodetector, memory, and photomemory, and the corresponding operating conditions of the perovskite bilayer memory. It should be noted that the schematic is simplified, and the specific range of operating conditions may vary with the device parameters, but the trend should be general for this kind of device. I_0 is the smallest detective light intensity (normally smaller than 10 nW cm^{-2} for perovskite-based photodetectors),[80,81] and V_3 is the breakdown voltage (dark gray areas), usually around 4 V. In general, the applied voltage can produce a wider range of device performance than the light illumination although the latter is still capable of switching between different modes under certain bias conditions. The device is in memory mode when the voltage pulse is larger than V_2 (≈1.9 V) because the strong electric field can easily trigger the formation of conducting filaments. On the other hand, when the voltage pulse is smaller than V_1 (≈0.2 V), the weak electric field could hardly move the halide vacancies or metal ions, and the device is in the photodetector mode.

The photomemory mode can be observed if $V_1 < V < V_2$ when the applied external illumination and voltage pulse are able to trigger the migration and accumulation of charged ions, but not strong enough to form any robust conducting filaments. The operation mechanism is schematically depicted in Figure S17 (Supporting Information). In this mode, clusters of accumulated ions remain after removing the light illumination, so that the current cannot immediately return to the original level and the resistance, giving rise to the photomemory functionality. Notably, under this circumstance, if the light intensity is gradually increased, the formed filaments will become more and more robust so that the device can convert from the photomemory mode to the memory mode. In other words, light irradiation can decrease the memory's threshold setting voltage, as illustrated in Figure 6d.

3. Conclusion

In conclusion, we have fabricated a multistate all-perovskite RS memory with a UV–visible dual light response by combining solution-processed oxide perovskite STO QDs' film and halide perovskite CPB thin film. Compared with the single-layer STO and the CPB RS memory devices, the double-layer device exhibits considerably improved RS performance with a high switching ratio of over 10^5, an endurance of 3000 cycles, and a retention time of longer than 2×10^4 s, and the photonic RS device consistently presents a distinct UV–visible dual light response. In addition, a unique tri-mode operation (i.e., memory, photodetector, and photomemory) has been demonstrated under tailored light and electric conditions. This work provides a new heterostructure-based strategy for enhancing the photoresponse of conventional oxide perovskite optoelectronics as well as stabilizing the performance of emerging halide perovskite devices.

Supporting Information

Supporting Information is available from the Wiley Online Library or from the author.

Conflict of Interest

The authors declare no conflict of interest.

Data Availability Statement

The data that support the findings of this study are available from the corresponding author upon reasonable request.

[1] Q. Cao, W. Lu, X. R. Wang, X. Guan, L. Wang, S. Yan, T. Wu, X. Wang, *ACS Appl. Mater. Interfaces* **2020**, *12*, 42449.

[2] J. Y. Mao, L. Zhou, X. Zhu, Y. Zhou, S. T. Han, *Adv. Opt. Mater.* **2019**, *7*, 1900766.

[3] W.-J. Yin, B. Weng, J. Ge, Q. Sun, Z. Li, Y. Yan, *Energy Environ. Sci.* **2019**, *12*, 442.

[4] D. Ji, S. Cai, T. R. Paudel, H. Sun, C. Zhang, L. Han, Y. Wei, Y. Zang, M. Gu, Y. Zhang, W. Gao, H. Huyan, W. Guo, D. Wu, Z. Gu, E. Y. Tsymbal, P. Wang, Y. Nie, X. Pan, *Nature* **2019**, *570*, 87.

**ADVANCED
SCIENCE NEWS**

www.advancedsciencenews.com

**ADVANCED
FUNCTIONAL
MATERIALS**

www.afm-journal.de

[5] Z. Fan, K. Sun, J. Wang, *J. Mater. Chem. A* **2015**, *3*, 18809.

[6] K. Ueno, S. Nakamura, H. Shimotani, A. Ohtomo, N. Kimura, T. Nojima, H. Aoki, Y. Iwasa, M. Kawasaki, *Nat. Mater.* **2008**, *7*, 855.

[7] S. Ouyang, H. Tong, N. Umezawa, J. Cao, P. Li, Y. Bi, Y. Zhang, J. Ye, *J. Am. Chem. Soc.* **2012**, *134*, 1974.

[8] H. J. Chung, J. H. Kim, S. I. Woo, *Chem. Mater.* **2001**, *13*, 1441.

[9] J. Xing, K. Zhao, H. Lu, X. Wang, G. Liu, K. Jin, M. He, C. Wang, G. Yang, *Opt. Lett.* **2007**, *32*, 2526.

[10] L. Wang, K.-j. Jin, J. Xing, C. Ge, H.-b. Lu, W.-j. Zhou, G.-z. Yang, *Appl. Opt.* **2013**, *52*, 3473.

[11] W. Yang, Y. Zhang, Y. Zhang, W. Deng, X. Fang, *Adv. Funct. Mater.* **2019**, *29*, 1905923.

[12] J. Xing, C. Zhao, E. Guo, F. Yang, *IEEE Sens. J.* **2012**, *12*, 2561.

[13] P. C. Joshi, S. B. Krupanidhi, *J. Appl. Phys.* **1993**, *73*, 7627.

[14] K. Szot, R. Dittmann, W. Speier, R. Waser, *Phys. Status Solidi RRL* **2007**, *1*, R86.

[15] T. Sakuma, S. Yamamichi, S. Matsubara, H. Yamaguchi, Y. Miyasaka, *Appl. Phys. Lett.* **1990**, *57*, 2431.

[16] X. Xu, Z. Wang, S. Lopatin, M. A. Quevedo-Lopez, H. N. Alshareef, *2D Mater.* **2018**, *6*, 015030.

[17] T. Wan, B. Qu, H. Du, X. Lin, P. Guan, Q. Lin, N. Chen, T. Teck Tan, T. Hang, D. Chu, *J. Colloid Interface Sci.* **2017**, *494*, 178.

[18] W. L. Harrigan, S. E. Michaud, K. A. Lehuta, K. R. Kittilstved, *Chem. Mater.* **2016**, *28*, 430.

[19] T. Wan, B. Qu, H. Du, X. Lin, Q. Lin, D. W. Wang, C. Cazorla, S. Li, S. Liu, D. Chu, *J. Colloid Interface Sci.* **2018**, *512*, 767.

[20] M. M. Lee, J. Teuscher, T. Miyasaka, T. N. Murakami, H. J. Snaith, *Science* **2012**, *338*, 643.

[21] F. Li, W. Yu, X. Guan, T. Wu, *Acc. Mater. Res.* **2021**, https://doi.org/10.1021/accountsmr.1c00103.

[22] S. D. Stranks, G. E. Eperon, G. Grancini, C. Menelaou, M. J. Alcocer, T. Leijtens, L. M. Herz, A. Petrozza, H. J. Snaith, *Science* **2013**, *342*, 341.

[23] D. Shi, V. Adinolfi, R. Comin, M. Yuan, E. Alarousu, A. Buin, Y. Chen, S. Hoogland, A. Rothenberger, K. Katsiev, Y. Losovyj, X. Zhang, P. A. Dowben, O. F. Mohammed, E. H. Sargent, O. M. Bakr, *Science* **2015**, *347*, 519.

[24] M. Liu, M. B. Johnston, H. J. Snaith, *Nature* **2013**, *501*, 395.

[25] H. Zhou, Q. Chen, G. Li, S. Luo, T. B. Song, H. S. Duan, Z. Hong, J. You, Y. Liu, Y. Yang, *Science* **2014**, *345*, 542.

[26] W. Nie, H. Tsai, R. Asadpour, J. C. Blancon, A. J. Neukirch, G. Gupta, J. J. Crochet, M. Chhowalla, S. Tretiak, M. A. Alam, H. L. Wang, A. D. Mohite, *Science* **2015**, *347*, 522.

[27] L. Duan, L. Hu, X. Guan, C.-H. Lin, D. Chu, S. Huang, X. Liu, J. Yuan, T. Wu, *Adv. Energy Mater.* **2021**, *11*, 2100354.

[28] C. Ma, Y. Shi, W. Hu, M. H. Chiu, Z. Liu, A. Bera, F. Li, H. Wang, L. J. Li, T. Wu, *Adv. Mater.* **2016**, *28*, 3683.

[29] R. Dong, Y. Fang, J. Chae, J. Dai, Z. Xiao, Q. Dong, Y. Yuan, A. Centrone, X. C. Zeng, J. Huang, *Adv. Mater.* **2015**, *27*, 1912.

[30] Y. Lee, J. Kwon, E. Hwang, C. H. Ra, W. J. Yoo, J. H. Ahn, J. H. Park, J. H. Cho, *Adv. Mater.* **2015**, *27*, 41.

[31] M. I. Saidaminov, M. A. Haque, M. Savoie, A. L. Abdelhady, N. Cho, I. Dursun, U. Buttner, E. Alarousu, T. Wu, O. M. Bakr, *Adv. Mater.* **2016**, *28*, 8144.

[32] X. Guan, X. Yu, D. Periyanagounder, M. R. Benzigar, J. K. Huang, C. H. Lin, J. Kim, S. Singh, L. Hu, G. Liu, D. Li, J. H. He, F. Yan, Q. J. Wang, T. Wu, *Adv. Opt. Mater.* **2020**, *9*, 2001708.

[33] C. Y. Kang, C. H. Lin, C. H. Lin, T. Y. Li, S. W. Huang Chen, C. L. Tsai, C. W. Sher, T. Z. Wu, P. T. Lee, X. Xu, *Adv. Sci.* **2019**, *6*, 1902230.

[34] G. Xing, N. Mathews, S. S. Lim, N. Yantara, X. Liu, D. Sabba, M. Gratzel, S. Mhaisalkar, T. C. Sum, *Nat. Mater.* **2014**, *13*, 476.

[35] H. Zhu, Y. Fu, F. Meng, X. Wu, Z. Gong, Q. Ding, M. V. Gustafsson, M. T. Trinh, S. Jin, X. Y. Zhu, *Nat. Mater.* **2015**, *14*, 636.

[36] F. Li, C. Ma, H. Wang, W. Hu, W. Yu, A. D. Sheikh, T. Wu, *Nat. Commun.* **2015**, *6*, 8238.

[37] A. Younis, C.-H. Lin, X. Guan, S. Shahrokhi, C.-Y. Huang, Y. Wang, T. He, S. Singh, L. Hu, J. R. D. Retamal, J. H. He, T. Wu, *Adv. Mater.* **2021**, *33*, 2005000.

[38] X. Guan, W. Hu, M. A. Haque, N. Wei, Z. Liu, A. Chen, T. Wu, *Adv. Funct. Mater.* **2018**, *28*, 1704665.

[39] Y. Shan, Z. Lyu, X. Guan, A. Younis, G. Yuan, J. Wang, S. Li, T. Wu, *Phys. Chem. Chem. Phys.* **2018**, *20*, 23837.

[40] X. Guan, Y. Wang, C.-H. Lin, L. Hu, S. Ge, T. Wan, A. Younis, F. Li, Y. Cui, D.-C. Qi, D. Chu, X. D. Chen, T. Wu, *Appl. Phys. Rev.* **2020**, *7*, 031401.

[41] M. Kulbak, S. Gupta, N. Kedem, I. Levine, T. Bendikov, G. Hodes, D. Cahen, *J. Phys. Chem. Lett.* **2016**, *7*, 167.

[42] Q. V. Le, J. W. Lee, W. Sohn, H. W. Jang, J. K. Kim, S. Y. Kim, *Cryst. Growth Des.* **2018**, *18*, 3161.

[43] S. G. Kim, Q. Van Le, J. S. Han, H. Kim, M. J. Choi, S. A. Lee, T. L. Kim, S. B. Kim, S. Y. Kim, H. W. Jang, *Adv. Funct. Mater.* **2019**, *29*, 1906686.

[44] S. Ge, Y. Wang, Z. Xiang, Y. Cui, *ACS Appl. Mater. Interfaces* **2018**, *10*, 24620.

[45] Y. Wang, Z. Lv, Q. Liao, H. Shan, J. Chen, Y. Zhou, L. Zhou, X. Chen, V. A. L. Roy, Z. Wang, Z. Xu, Y. J. Zeng, S. T. Han, *Adv. Mater.* **2018**, *30*, 1800327.

[46] Z. Li, Z. Li, Z. Shi, X. Fang, *Adv. Funct. Mater.* **2020**, *30*, 2002634.

[47] L. Li, Z. Lou, G. Shen, *Adv. Funct. Mater.* **2017**, *28*, 1705389.

[48] D. Hao, D. Liu, Y. Shen, Q. Shi, J. Huang, *Adv. Funct. Mater.* **2021**, *31*, 2100773.

[49] T. T. Huang, W. Wu, *Adv. Mater. Interfaces* **2020**, *7*, 2000015.

[50] Z. Chen, Y. Guo, E. Wertz, J. Shi, *Adv. Mater.* **2019**, *31*, 1803514.

[51] L. Yang, M. Singh, S. W. Shen, K. Y. Chih, S. W. Liu, C. I. Wu, C. W. Chu, H. W. Lin, *Adv. Funct. Mater.* **2020**, *31*, 2008259.

[52] L. Hu, J. Yuan, Y. Ren, Y. Wang, J. Q. Yang, Y. Zhou, Y. J. Zeng, S. T. Han, S. Ruan, *Adv. Mater.* **2018**, *30*, 1801232.

[53] X. Guan, Z. Wang, M. K. Hota, H. N. Alshareef, T. Wu, *Adv. Electron. Mater.* **2019**, *5*, 1800538.

[54] Y. Hao, X. Wang, L. Li, *Nanoscale* **2014**, *6*, 7940.

[55] D. Bao, X. Yao, N. Wakiya, K. Shinozaki, N. Mizutani, *Appl. Phys. Lett.* **2001**, *79*, 3767.

[56] K. Xu, M. Yao, J. Chen, P. Zou, Y. Peng, F. Li, X. Yao, *J. Alloys Compd.* **2015**, *653*, 7.

[57] E. Yoo, M. Lyu, J. H. Yun, C. Kang, Y. Choi, L. Wang, *J. Mater. Chem. C* **2016**, *4*, 7824.

[58] Y. Sun, M. Tai, C. Song, Z. Wang, J. Yin, F. Li, H. Wu, F. Zeng, H. Lin, F. Pan, *J. Phys. Chem. C* **2018**, *122*, 6431.

[59] S. Ge, X. Guan, Y. Wang, C.-H. Lin, Y. Cui, Y. Huang, X. Zhang, R. Zhang, X. Yang, T. Wu, *Adv. Funct. Mater.* **2020**, *30*, 2002110.

[60] Y. Cui, H. Peng, S. Wu, R. Wang, T. Wu, *ACS Appl. Mater. Interfaces* **2013**, *5*, 1213.

[61] J. Choi, Q. V. Le, K. Hong, C. W. Moon, J. S. Han, K. C. Kwon, P. R. Cha, Y. Kwon, S. Y. Kim, H. W. Jang, *ACS Appl. Mater. Interfaces* **2017**, *9*, 30764.

[62] J. Y. Seo, J. Choi, H. S. Kim, J. Kim, J. M. Yang, C. Cuhadar, J. S. Han, S. J. Kim, D. Lee, H. W. Jang, N. G. Park, *Nanoscale* **2017**, *9*, 15278.

[63] J. S. Han, Q. V. Le, J. Choi, K. Hong, C. W. Moon, T. L. Kim, H. Kim, S. Y. Kim, H. W. Jang, *Adv. Funct. Mater.* **2018**, *28*, 1705783.

[64] A. Bera, K. Wu, A. Sheikh, E. Alarousu, O. F. Mohammed, T. Wu, *J. Phys. Chem. C* **2014**, *118*, 28494.

[65] Y. Hu, S. Zhang, X. Miao, L. Su, F. Bai, T. Qiu, J. Liu, G. Yuan, *Adv. Mater. Interfaces* **2017**, *4*, 1700131.

[66] Y. Wu, Y. Wei, Y. Huang, F. Cao, D. Yu, X. Li, H. Zeng, *Nano Res.* **2017**, *10*, 1584.

[67] C. Cuhadar, S. G. Kim, J. M. Yang, J. Y. Seo, D. Lee, N. G. Park, *ACS Appl. Mater. Interfaces* **2018**, *10*, 29741.

[68] H. An, W. K. Kim, C. Wu, T. W. Kim, *Org. Electron.* **2018**, *56*, 41.

[69] Z. Chen, Y. Zhang, Y. Yu, Y. Che, L. Jin, Y. Li, Q. Li, T. Li, H. Dai, J. Yao, *Opt. Mater.* **2019**, *90*, 123.

**ADVANCED
SCIENCE NEWS**

www.advancedsciencenews.com

**ADVANCED
FUNCTIONAL
MATERIALS**

www.afm-journal.de

[70] Z. Xiong, W. Hu, Y. She, Q. Lin, L. Hu, X. Tang, K. Sun, *ACS Appl. Mater. Interfaces* **2019**, *11*, 30037.

[71] H. Cai, M. Lao, J. Xu, Y. Chen, C. Zhong, S. Lu, A. Hao, R. Chen, *Ceram. Int.* **2019**, *45*, 5724.

[72] R. Chen, J. Xu, M. Lao, Z. Liang, Y. Chen, C. Zhong, L. Huang, A. Hao, M. Ismail, *Phys. Status Solidi RRL* **2019**, *13*, 1900397.

[73] J. S. Han, Q. V. Le, J. Choi, H. Kim, S. G. Kim, K. Hong, C. W. Moon, T. L. Kim, S. Y. Kim, H. W. Jang, *ACS Appl. Mater. Interfaces* **2019**, *11*, 8155.

[74] J.-Y. Mao, Z. Zheng, Z.-Y. Xiong, P. Huang, G.-L. Ding, R. Wang, Z.-P. Wang, J.-Q. Yang, Y. Zhou, T. Zhai, S.-T. Han, *Nano Energy* **2020**, *71*, 104616.

[75] F. Ma, Y. Zhu, Z. Xu, Y. Liu, X. Zheng, S. Ju, Q. Li, Z. Ni, H. Hu, Y. Chai, C. Wu, T. W. Kim, F. Li, *Adv. Funct. Mater.* **2020**, *30*, 1908901.

[76] E.-J. Guo, H.-B. Lu, M. He, J. Xing, K.-J. Jin, G.-Z. Yang, *Appl. Opt.* **2010**, *49*, 2557.

[77] H. Zhou, Z. Song, C. R. Grice, C. Chen, J. Zhang, Y. Zhu, R. Liu, H. Wang, Y. Yan, *Nano Energy* **2018**, *53*, 880.

[78] X.-L. Ou, M. Xu, J. Feng, H.-B. Sun, *Sol. Energy Mater. Sol. Cells* **2016**, *157*, 660.

[79] X. Zhu, J. Lee, W. D. Lu, *Adv. Mater.* **2017**, *29*, 1700527.

[80] Y. Fang, J. Huang, *Adv. Mater.* **2015**, *27*, 2804.

[81] L. Dou, Y. M. Yang, J. You, Z. Hong, W. H. Chang, G. Li, Y. Yang, *Nat. Commun.* **2014**, *5*, 5404.